Published in "Journal of Statistical Mechanics: Theory and Experiment 2016(9): 094003, 2016" which should be cited to refer to this work.

Dynamical and structural signatures of the glass transition in emulsions

Chi Zhang[1,6], Nicoletta Gnan[2,3,6], Thomas G Mason[4,5], Emanuela Zaccarelli[2,3] and Frank Scheffold[1]

[1] Department of Physics, University of Fribourg, Fribourg, Switzerland
[2] CNR-ISC UOS Sapienza, Piazzale A. Moro 2, 00185 Roma, Italy
[3] Department of Physics, Sapienza University of Rome, Piazzale A. Moro 2, 00185 Roma, Italy
[4] Department of Chemistry and Biochemistry, University of California-Los Angeles, Los Angeles, CA 90095, USA
[5] Department of Physics and Astronomy, University of California-Los Angeles, Los Angeles, CA 90095, USA
E-mail: frank.scheffold@unifr.ch and nicoletta.gnan@roma1.infn.it

Abstract. We investigate structural and dynamical properties of moderately polydisperse emulsions across an extended range of droplet volume fractions ϕ, encompassing fluid and glassy states up to jamming. Combining experiments and simulations, we show that when ϕ approaches the glass transition volume fraction ϕ_g, dynamical heterogeneities and amorphous order arise within the emulsion. In particular, we find an increasing number of clusters of particles having five-fold symmetry (i.e. the so-called locally favoured structures, LFS) as ϕ approaches ϕ_g, saturating to a roughly constant value in the glassy regime. However, contrary to previous studies, we do not observe a corresponding growth of medium-range crystalline order; instead, the emergence of LFS is decoupled from the appearance of more ordered regions in our system. We also find that the static correlation lengths associated with the LFS and with the fastest particles can be successfully related to the relaxation time of the system. By contrast, this does not hold for the length associated with the orientational order. Our study reveals the existence of a link between dynamics and structure close to the glass transition even in the absence of crystalline

[6] These authors contributed equally to this work.

precursors or crystallization. Furthermore, the quantitative agreement between our confocal microscopy experiments and Brownian dynamics simulations indicates that emulsions are and will continue to be important model systems for the investigation of the glass transition and beyond.

Keywords: colloidal glasses, glasses (colloidal, polymer, etc)

Contents

Emulsions are of great practical importance in pharmaceutical, cosmetics, food, and agrochemical products [1]. In addition to their utility from an engineering perspective, these systems are gaining renewed attention in soft matter physics as model system for soft colloids [2–5]. Indeed, thanks to the ability of constituent droplets to deform without coalescing and thereby increase their surface area, emulsions can pack well beyond the so called random close packing or jamming limit [6–8], which represents the maximal volume fraction of hard-spheres when they are packed in a disordered manner. Crossing into and beyond random close packing, emulsions undergo a transition toward an elastic amorphous solid in which the rearrangement of droplets is not possible, the

viscosity diverges and bulk samples exhibit a finite elastic shear modulus [4, 5, 9–14]. Together with the huge effort in characterizing the jamming transition, great attention has been devoted to the lower density regime where emulsions behave similarly to a colloidal viscous fluid, displaying a transition from an ergodic fluid state to a non-ergodic weak solid known as the glass transition [3, 14–19].

As a general feature, when the glass transition is approached, the viscosity of a material sharply increases and the dynamics dramatically slow down. These phenomena are accompanied by the emergence of dynamical heterogeneities in the collective rearrangement of particles [20–22]. Despite the presence of heterogeneous dynamics, structural quantities such as the radial distribution function $g(r)$ change very little suggesting the absence of large spatial correlations. The connection between structure and dynamics close to the glass transition is a debated issue which has been discussed in different theroretical frameworks [23–26]. More recently it has been shown that it is possible to link the heterogeneous dynamics of particles with peculiar structural arrangements arising within the system on approaching the dynamic arrest [19, 27–30]. The underlying idea is that regions of slow particle rearrangements must be connected to local structures which are energetically favorable. Such stable structures are thought to correspond to local minima of the energy landscape in which the system remains trapped. This is the picture proposed by Frank [31], who has identified locally favourable structures (LFS) in the Lennard-Jones system as structures with icosahedral order. LFS maximise the density of packing and thus are energetically favoured with respect to the equilibrium face-centered cubic (FCC) crystal structure of the Lennard-Jones system. In addition, geometric frustration introduced by their five-fold symmetry is incompatible with long-range order; hence, the presence of LFS has been conjectured to have a fundamental role in the vitrification process [32].

Other numerical and experimental studies have revealed that crystalline order may play a key role in the vitrification process even if crystallization is avoided. In this case there is an underlying reference crystalline state to which a specific bond orientational order (BOO) is associated. Simulations and experiments [33, 34] have shown that, although translational order is avoided, thereby suppressing crystal formation, bond orientational ordering is still present, and it actually grows upon cooling, extending up to medium range BOO. For the case of slightly polydisperse hard-spheres [34], it was shown that BOO is related to local dynamics, i.e. particles belonging to arrangements with high orientational order are less mobile. All of these findings suggest that the dynamic slowing down and the increasing dynamical heterogeneities towards the glass transition may have some structural bases.

Despite the growing interest in the packing of soft spheres over the last decade, emulsions have been largely underestimated as a quantitative model system. Few experimental works on emulsions have focused on the properties in the glassy and jammed regime under shear flow [3, 10, 11, 14], while the glassy behaviour of oil-in-water emulsions in the absence of flow has been studied only by dynamic light scattering [17]. The great advantage of emulsions is that the droplet volume fraction is well defined since the liquid within the droplet is incompressible even when particle deform. This makes them suitable candidates for a better comparison with numerical and theoretical descriptions both with respect to hard spheres, for which the packing fraction definition is often problematic [35], and to soft particles such as microgels or

star polymers that may deswell or interpenetrate [36–41]. Moreover solid friction and entanglements cannot play a role in emulsions, whereas they might in solid particulate or microgel dispersions.

In this work, we report an extensive study of the structural and dynamical properties of emulsions from states below the glass transition volume fraction up to jamming and we compare 3D fluorescent microscopy measurements with numerical simulations. We identify multiple signatures of the glass transition, analyzing both dynamical and structural quantities, highlighting a connection between the dynamic slowing down and growing dynamical and structural correlation lengths. This link is revealed by looking at the increasing population of LFS as well as of clusters of fast particles as the glass transition is approached. However, the relatively large polydispersity of our samples, beyond the known terminal polydispersity above which a single-phase crystallization can occur [42, 43], differentiates our system from previous studies, because of the absence of the growth of locally crystalline regions. Last but not least, we demonstrate quantitative agreement with numerical simulations, opening the pathway for future quantitative predictions for different soft repulsive particle systems over the entire range of concentrations from the fluid regime to the jammed regime.

1. Experimental methods

1.1. Sample preparation

We prepare stable uniform oil-in-water emulsions as described in [44]. We start with a $3:1$ mixture by weight of polydimethylsiloxane (PDMS; viscosity $15 \sim 45$ mPa·s, density $1.006\,\mathrm{g\,ml^{-1}}$) and polyphenylmethylsiloxane (PPMS-AR200; viscosity 200 mPa·s, density $1.05\,\mathrm{g\ ml^{-1}}$) and we emulsify it in a couette shear-cell with sodium dodecyl sulfate (SDS) surfactant in water for stabilizing the droplets. To remove evaporable short molecules the PDMS oils is placed in an oven at 60 °C overnight prior to emulsification. Depletion sedimentation [45] is then used to fractionate the droplets by size, until the desired polydispersity $PD \simeq 12\%$ is achieved in the sample. For such polydispersity we find the size distribution of droplets to be close to log-normal with a mean droplet radius $a = 1.05\ \mu$m or a droplet diameter $\sigma = 2.1\ \mu$m. To sterically stabilize the droplets, SDS is replaced by the block-copolymer surfactant Pluronic F108. In addition, formamide and dimethylacetamid (DMAC) are added to the solvent in order to simultaneously match the solute-solvent density and the refractive index at room temperature $T = 22$ °C. Finally, the fluorescent dye Nile red is added to the solution in order to obtain optical contrast between the droplet and the dispersion medium. Several hundred microliters of sample are spun down marginally above jamming with centrifugation. The latter is carried out at 4 °C in order to induce a slight density mismatch between the droplets and the solvent. The stock sample then is diluted continuously in steps of 0.5%. After each dilution, we put a small amount of suspension in an evaporation-proof cylindrical cell of diameter $d = 2\,$mm and heigth $h = 120\ \mu$m sealed with UV-glue to a microscope cover slip.

1.2. Image acquisition

3D High-resolution images of droplets are obtained using a laser-scanning confocal microscopy module, Nikon A1R, controlled by Nikon Elements software. Images are acquired with a X60 oil immersion objective with zoom X2. Although the dye is present both in the continous phase and in the dispersed oil droplets, the emission spectra are different, exhibiting emission peaks of 670 nm and 580 nm for the continuous phase and for the oil, respectively, when the sample is excited with a 488 nm laser. The dimension of the recorded images are $512 \times 512 \times 101$ pixels with a resolution of 0.21 μm/pixel in each direction. Droplets are reconstructed by a template based particle tracking method known as the sphere matching method (SMM) [46] and Voronoi radical tessellation [47] to identify neighbors of each particle. In our case the accuracy of the coordinates is roughly 20 nm in the lateral direction and 35 nm in the vertical direction. The accuracy of the size determined from the analysis of immobile droplets is about 20 nm. Due to the finite exposure time, the size of droplets extracted from the tracking algorithm is slightly different for samples having different volume fractions, due to motion blurring of droplets in the images. Since all samples are made out of the same stock suspension, we assume that the particle size distribution for different samples is the same. We proceed in the following way: first the particle size distribution of the system is measured at random close packing assuming $\phi_J = 64.2\%$, which corresponds to the value found for marginally jammed polydisperse frictionless spheres with polydispersity $PD \simeq 12\%$ [44, 48]. This size distribution is fixed throughout. Next, the particle size distributions obtained from the SMM tracking algorithm at lower concentrations are calibrated using this reference distribution, and, in this way, the volume fraction of each sample is determined.

The fact that we can reversibly jam the system provides a well defined benchmark. In turn, we obtain a much better estimate for the absolute values of the packing fraction as compared to hard sphere systems [35]. We estimate the absolute accuracy of our ϕ-values to be better than 0.5% with a statistical error better than 0.3%. The small difference is due to the finite accuracy with respect to ϕ_J [44, 48].

2. Simulation methods

To model the behaviour of dense emulsions we use a soft repulsive potential, following previous works [2, 14, 49–52] which have shown how the elastic and dynamic properties across the glass and the jamming transitions depend not only on the volume fraction ϕ but also on the strength of the repulsion. We thus model emulsions as particles interacting with a harmonic potential

$$\beta U(r_{ij}) = u_0 \left(1 - r/\sigma_{ij}\right)^2 \Theta\left(r_{ij} - \sigma_{ij}\right) \tag{1}$$

where i,j is the index of two particles with diameter σ_i and σ_j (with $\sigma_{ij} = 0.5(\sigma_i + \sigma_j)$) and u_0 is proportional to the harmonic spring constant and is in units of $k_{\mathrm{B}}T$. The length unit is chosen to be the average colloid diameter $\langle\sigma\rangle$ and time t is in units of $\langle\sigma\rangle\sqrt{m/u_0}$ (reduced units) where m is the mass of a single particle. We perform Brownian dynamics (BD) simulations of $N = 2000$ polydisperse particles; a velocity Verlet integrator is

used to integrate the equations of motion with a time step $\mathrm{d}t = 10^{-4}$. We follow [53] to model Brownian diffusion by defining the probability p that a particle undergoes a random collision every X time-steps for each particle. By tuning p it is possible to obtain the desired free particle diffusion coefficient $D_0 = (k_\mathrm{B}TX\mathrm{d}t/m)(1/p - 1/2)$. We fix $D_0 = 0.0081$ in reduced units, for which the crossover from ballistic to diffusive regime, for isolated particles, takes place at $t \sim 0.01$.

Using a harmonic approximation for the interaction potential is reasonable for small deformations of the droplets [49, 54]. Here, we consider only concentrations at or below jamming $\phi \leqslant \phi_J = 64.2\%$ [44] and thus deformations can be considered small and the harmonic potential approximately applies. As discussed in a previous work [14], the value of u_0 is set by the surface tension of the system. Indeed a 1% change in volume fraction above random close packing corresponds to a droplet compression $(1 - r/\sigma)^2 = 2.7 \cdot 10^{-5}$, thus as long as u_0 is much larger than $10^5\, k_\mathrm{B}T$ the energy cost to thermally induce a corresponding shape fluctuation is $\gg k_\mathrm{B}T$. Based on these considerations, we set $u_0 = 1.0 \cdot 10^7$, which also matches rheology data [14][7]. For such values of u_0, the system under study is hard enough to be considered almost as hard-spheres, since the droplet deformation due to thermal fluctuations is very small. Nonetheless, the softness of the droplets and the absence of friction are key properties of emulsions that allow for the preparation of dense and marginally jammed systems. The polydispersity of the system is described by a log-normal distribution with unitary mean and standard deviation equal to $PD = 12\%$ following the experimental probability size distribution. The total simulation time for all the volume fractions investigated ranges between $5.5 \cdot 10^7$ and $2.4 \cdot 10^8$ BD steps, corresponding to $t \in [5.5 \cdot 10^3, 2.4 \cdot 10^4]$ in reduced units. A recent numerical work on HS with polydispersity $\simeq$12% [55] has shown that the relaxation features of the system depends very much on the population of small and large particles belonging to the tails of the size distribution. In the HS system, aging also affects fully decaying intermediate scattering functions (ISF) when $\phi > 59\%$, which depend not only on the observation time t but also on the waiting time t_w, i.e. the time elapsed from the beginning of the experiment or simulation. Due to polydispersity, it was found that small and large particles undergo a dynamical arrest at different packing fractions; while large HS particles are dynamically arrested already at $\phi = 58\%$, small particles are still free to move in the matrix formed by the large particles. For our emulsions, we observe a similar behavior, finding that the system starts to display aging for $\phi > 58.1\%$. This is shown in figure 1(a) where the self ISF defined as $F_s(\vec{q}, t) = (1/N)\sum_{1=1}^{N} \mathrm{e}^{\mathrm{i}\vec{q}\cdot(\vec{r}_i(0) - \vec{r}_i(t))}$ is displayed at different waiting times for $\phi = 58.1\%$ and $\phi = 58.5\%$ and wave vector $\vec{q}$ roughly corresponding to the position of the first peak of the structure factor $S(q)$. Hence, for $\phi > 58.1\%$ we consider the system to be out-of-equilibrium.

3. Comparison between numerical and experimental data

Using Brownian dynamics (BD), rather than molecular dynamics (MD), in the simulation method is advantageous, because BD yields more accurate microscopic dynamics

[7] Oscillatory shear measurements of our emulsions (data not shown) indicate a surface tension of 0.01–0.015 Nm^{-1} and thus $u_0 \sim 2$–$3 \times 10^7 k_\mathrm{B}T$ [14].

of emulsion droplets, thereby enabling us to achieve very good quantitative agreement between numerical and experimental dynamical observables, such as the mean square displacement, over an extended dynamic range in time. The use of MD simulations would have only allowed us to compare the resulting transport coefficients, such as the long-time diffusion coefficient D, although with better numerical efficiency in terms of computational time. By contrast to other systems [55], the determination of the packing fraction does not require any adjustable free parameter, and we directly use the experimental values in the simulations. In order to improve the agreement reported with experimental data, we had to account in simulations for the error in the experimental exposure time, which is a source of noise in the coordinates along the three axis in confocal microscopy measurements. In fact, the scan over a single particle takes on average 1s, a time in which the particle is free to explore a certain volume within the cage. As a consequence, the coordinates of particles extracted are affected by a noise that results in a suppression of the peak of the $g(r)$ [37]. Since the short time motion for samples with different volume fraction is different, we would expect different level of noise on increasing ϕ. An estimate of how much a particle with average radius $a \sim 1$ μm has moved in 1 s is given by the cage size which can be approximately written as [56, 57] $\epsilon = 4a[(\phi_J/\phi)^{1/3} - 1]$. In addition to that, we consider the accuracy of the particle tracking. This brings an error of roughly $\delta_{\rm track} \simeq 0.1$ pixel (with 1 pixel $\simeq$0.2 μm) in the lateral direction and $\delta_{\rm track} \simeq 0.15$ pixel in the axial directions. Basing on such consideration, the noise can be approximately estimated as a Gaussian distribution $P(0, \epsilon^2 + \delta^2_{\rm track})$ with zero mean and variance $w = \epsilon^2 + \delta^2_{\rm track}$. We apply such Gaussian noise to the three coordinates of all the particles in simulations, finding a very good agreement with experimental results.

4. Results

4.1. Dynamical properties close to the glass transition

4.1.1. Mean square displacement and α-relaxation We start our discussion by showing the dynamical properties of emulsions in experiments and simulations around the glass transition volume fraction. Figure 1(b) shows the comparison between the two sets of data for the mean square displacement $\langle \delta r^2 \rangle = (1/N) \sum_i |\vec{r}_i(0) - \vec{r}_i(t)|^2$. As for most of molecular liquids and colloidal systems, the dynamics shows a dramatic slowing down on approaching ϕ_g and $\langle \delta r^2 \rangle$ displays the emergence of a typical plateau associated to the presence of 'cages' in which particles remain trapped for an increasingly long time. We find that a simple model such as harmonic spheres quantitatively captures the dynamical behaviour of emulsions in an extended time region covering more than two decades for a wide range of packing fractions at and below jamming. Note that to superimpose experimental and numerical data a shift in time has been applied to the numerical mean square displacement. From the long-time limit of numerical mean square displacements we can extract the diffusion coefficient using the Einstein relation $D = \langle \delta r^2 \rangle / 6t$. For experiments, we could not reach a purely diffusive long-time regime, thus we estimate D by introducing a relaxation time $\tau_{\rm D}$, through the empirical relation $\langle \delta r^2 \rangle = 3(1 + t/\tau_{\rm D})\epsilon^2$

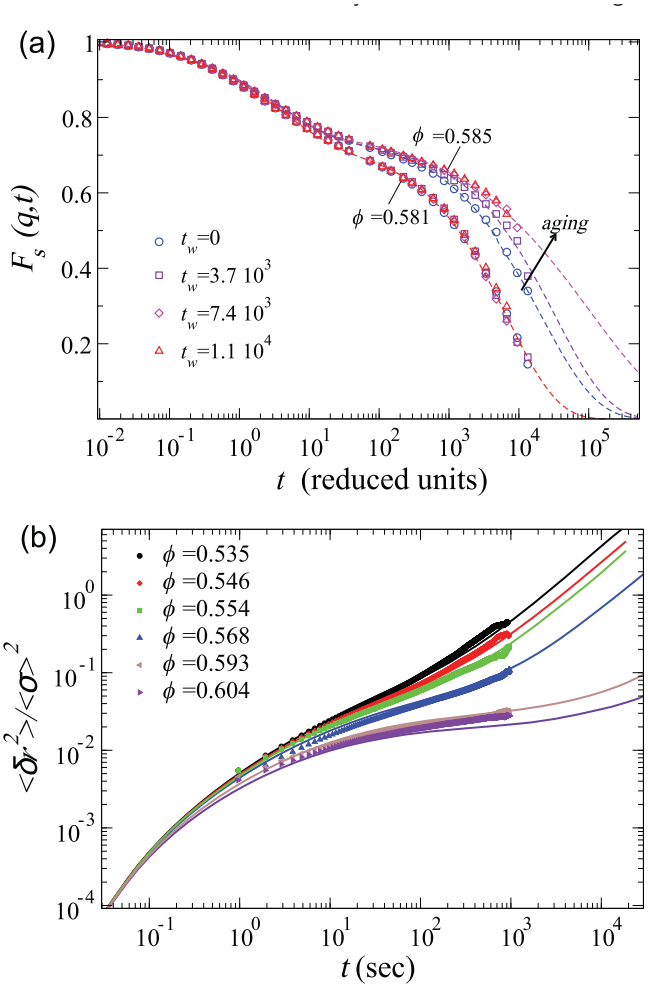

Figure 1. (a) Self intermediate scattering function (ISF) for two droplet volume fractions $\phi = 58.1\%$ and $\phi = 58.5\%$ evaluated at different waiting times t_w and $q\langle\sigma\rangle \simeq 7.2$. While for $\phi = 58.1\%$ no aging effects are observed, for $\phi = 58.5\%$ an increase of the relaxation time of the self ISF as a function of t_w is not negligible. Dashed lines are guides to the eye. (b) Normalized mean square displacements. Droplet volume fractions range from 53.5% to 60.4%. Symbols are data from confocal microscopy measurements; lines are results from Brownian dynamics simulations. Note that the simulation curves have been shifted on the time-axis by the same arbitrary factor to match the experimental microscopic timescale.

[58] where ϵ is the characteristic cage size. The derivation of such expression is found in appendix A. The associated diffusion coefficient is defined as $D = 3\epsilon^2/\tau_D$. The resulting numerical and experimental D and τ_D are shown in figure 2. The diffusion coefficient is represented in the figure 2(a), showing no difference on the way it has been calculated (Einstein or empirical relation). We also notice that the results are in good agreement with previous numerical data for a HS sphere system with the same polydispersity [55] that we plot together with results from emulsions, to show that our system behaves almost as HS. By performing a power-law fit $D \propto |\phi - \phi_g|^\gamma$ we find that $\phi_g = 58.9\%$ and $\gamma = 2.29$ for experiments, while $\phi_g = 59.1\%$ and $\gamma = 2.12$ for simulations, which are both in good agreement with power-law fits of [55]. However, differently from HS simulations,

we do not observe a deviation from a power-law decay in our numerical study; this is because Brownian dynamics is slower than molecular dynamics and does not allow to probe, within the same simulation time, the time scales that can be explored with MD. Hence, the values of ϕ that we consider are much further away from ϕ_g, as compared to [55], for any deviation to be observed. The relaxation time τ_D is shown in figure 2(b); a power-law fit of τ_D as a function of ϕ, gives similar results for ϕ_g and γ. A slightly higher value of $\phi_g \simeq 61.6\%$ is obtained if data are instead interpolated with the empirical Vogel–Fulcher–Tammann (VFT) expression

$$\tau_D = \exp(A\phi_g/|\phi - \phi_g|). \tag{2}$$

The small difference between the results of the two interpolations is again a consequence of the fact that both numerical and experimental results are too far from ϕ_g to observe a difference between the interpolating relations and discern which is the the best between the two. The two fits (power law and exponential) for the experimental data set are shown also in the figure. Finally we want to point out the difference between the numerical τ_D and the α-relaxation time τ_α extracted from the self ISF from simulations which are both shown in the same panel (dashed and dash-dotted lines); we find that the two times can be superimposed for a wide range of packing fractions, but start to show a decoupling on approaching the glass transition, a signature of the the violation of the Stokes-Einstein relation occurring between D and τ_α close to ϕ_g.

4.1.2. Dynamical heterogeneity One common way to characterize dynamic heterogeneities is to look for deviations of the particle displacements compared to free diffusion [20, 59]. For a random diffusion process the displacement distribution $P(\Delta x, t)$ at a given time t is a Gaussian with zero mean and a variance equal to the mean square displacement. Collective and correlated displacements lead to dynamic heterogeneities and deviations from the Gaussian distribution as shown in figure 3(a). Such deviations can be quantified by a non-Gaussian parameter defined as:

$$\alpha_2 = \frac{3\langle \delta r^4 \rangle}{5\langle \delta r^2 \rangle^2} - 1. \tag{3}$$

In figure 3(b) we plot α_2 as a function of the particle mean square displacement. Initially the values are nearly zero in the liquid but acquire appreciable values when approaching the glass transition volume fraction. In this regime α_2 displays a pronounced peak. This is because the movement of particles results from the combination of the intra-cage and inter-cage dynamics. At short time scales, the displacement is mostly due to intra-cage dynamics and the distribution is nearly Gaussian $\alpha_2 \sim 0$. Collective rearrangements are associated with cage breaking in the glass. Thus the peak in α_2 is related to the size of the cage. As the cage size gets compressed the maximum of α_2 is shifted towards smaller values of $\langle \delta r^2 \rangle$. At long times, or large values of $\langle \delta r^2 \rangle$, the displacements are due to a sum of many random cage breaking processes and the distribution becomes Gaussian again.

Another interesting way to analyze the collective particle motion is to look specifically at a of particles that differ from the Gaussian. Following [20] we define the population of fast particles as the 5% most mobile particles within a certain time interval, calculated with respect to $t = 0$. The ratio of 5% is chosen based on the fact that the

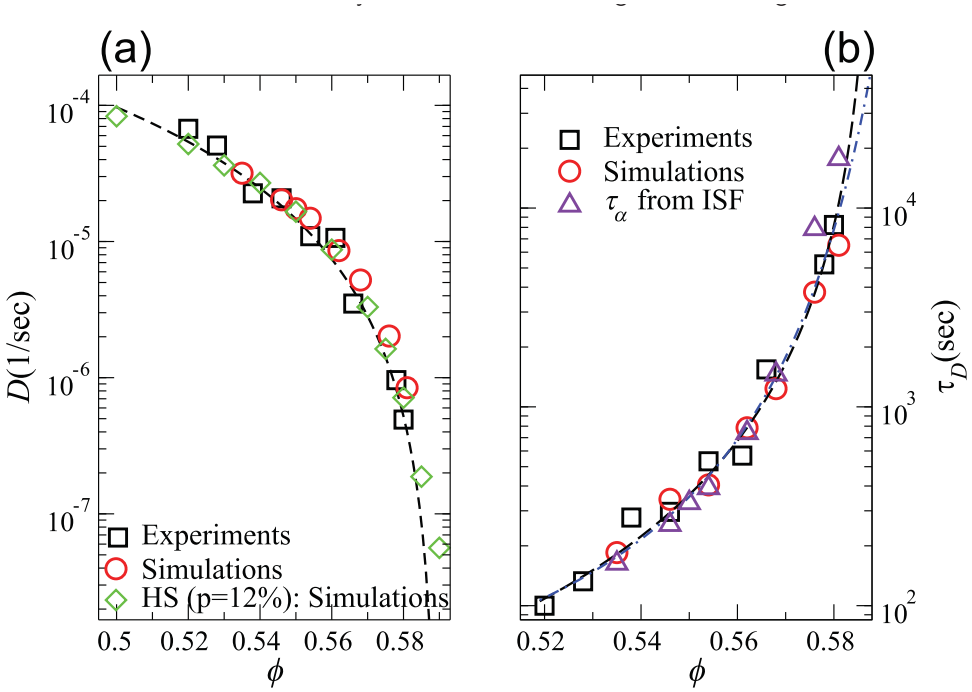

Figure 2. (a) Diffusion coefficient D as a function of the volume fraction ϕ for experiments (open squares) and simulations (open circles). Open diamonds are numerical results for HS particles with polydispersity $PD = 12\%$ from [55]. Note that numerical D values have been shifted by an arbitrary factor to match the experimental results for emulsions. The dashed line is the power-law fit of the experimental data set which gives $\phi_g = 58.9\%$ and $\gamma = 2.29$. The same interpolation for numerical data gives $\phi_g = 59.1\%$ and $\gamma = 2.12$; (b) relaxation time τ_D extracted from the mean square displacement for both experiments (open squares) and simulations (open circles). A power-law fit of the two data sets gives, respectively, $\phi_g = 58.9\%$ and $\gamma = 2.1$ for experiments and $\phi_g = 59.1\%$ and $\gamma = 2.1$ for simulations. By interpolating experimental data with the VFT relation we obtain $\phi_g = 61.6\%$. The two interpolating lines for experimental data are shown in the figure (dashed lines). For comparison we also show the relaxation time τ_α extracted from the numerical self ISF (open triangles). As in the left panel, numerical data have been shifted by an arbitrary factor. We find that τ_α starts to decouple from the numerical τ_D on approaching the glass transition packing fraction.

percentage of particles whose displacement deviates from a Gaussian distribution is roughly 5% (figure 3(a)) [59, 60]. Figure 4 shows several snapshots of fast particles that are spatially correlated. The appearance of spatial correlations is direct evidence for dynamic heterogeneities close to the glass transition [20, 61]. We define clusters of i particles from set of fast neighbouring particles identified via the Voronoi radical tessellation. The mean cluster size of fast particles is defined by taking the sum over clusters of all sizes and averaging over several configurations. The values for $\langle N_c \rangle$ we find depend both on concentration and on time. The latter is shown in figure 4. Especially close to ϕ_g, $\langle N_c \rangle$ displays a pronounced maximum as a function of time. Moreover, this maximum is located close to the relaxation time τ_D. Away from ϕ_g the peak is not pronounced or even absent. This suggests that, on approaching ϕ_g, collective rearrangements play a

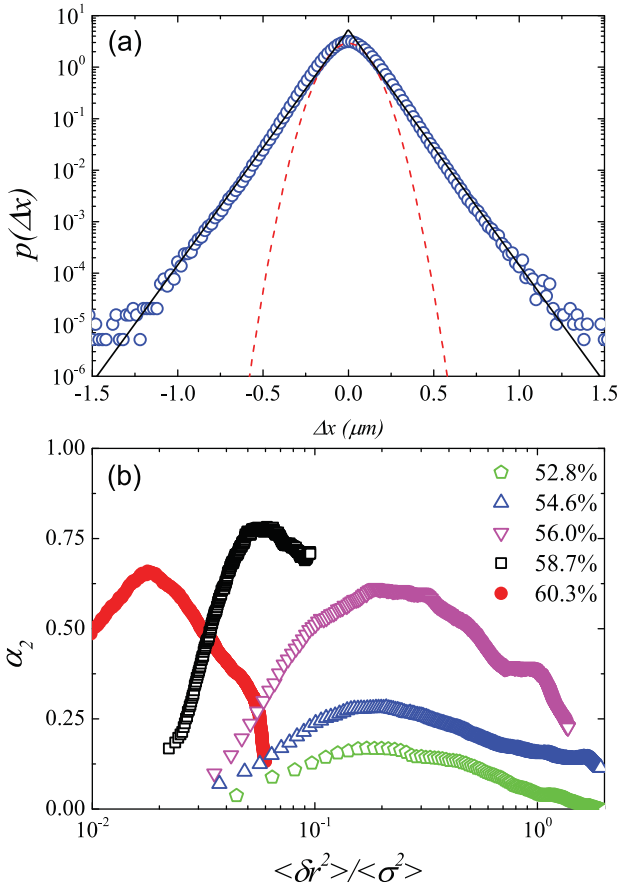

Figure 3. Experimental measurements of non-Gaussian step-size distributions and dynamical heterogeneities for ϕ near and above ϕ_g. (a) Distribution of droplet displacements Δx obtained from confocal microscopy at a volume fraction of $\phi = 60.3\%$ and time $t = 2160\,\mathrm{s}$. Dashed line: best fit of the peak center to a Gaussian distribution; solid line: best fit of the tails to a stretched exponential distribution. (b) Non-Gaussian parameter α_2 as a function of the dimensionless mean square displacement for volume fractions from 52.8% to 60.3%.

increasingly important role. By selecting the maximum value of $\langle N_c \rangle$ for several volume fractions, we can plot the concentration dependence of the cluster size $\langle N_c \rangle_{\max}$ (In the absence of a clear maximum we select an arbitrary time). As shown in figures 4(b) and (c) the cluster size increases on approaching the glass transition and then decreases above ϕ_g. This behaviour is observed both for simulations and experiments as shown in figure 4(a). We note that due to the polydispersity of the system small particles tend to be more mobile than larger particles. In connection to this it is worthwhile mentioning that the average size of the fast particle population is smaller, e.g. for $\phi = 59.3\%$, the mean radius of fast particles is around 0.92 μm, while for all particles it is 1.05 μm.

4.2. Structural properties close to the glass transition

4.2.1. Radial distribution function Figure 5(a) shows the radial distribution functions of the system for three different packing fractions taken from experiments

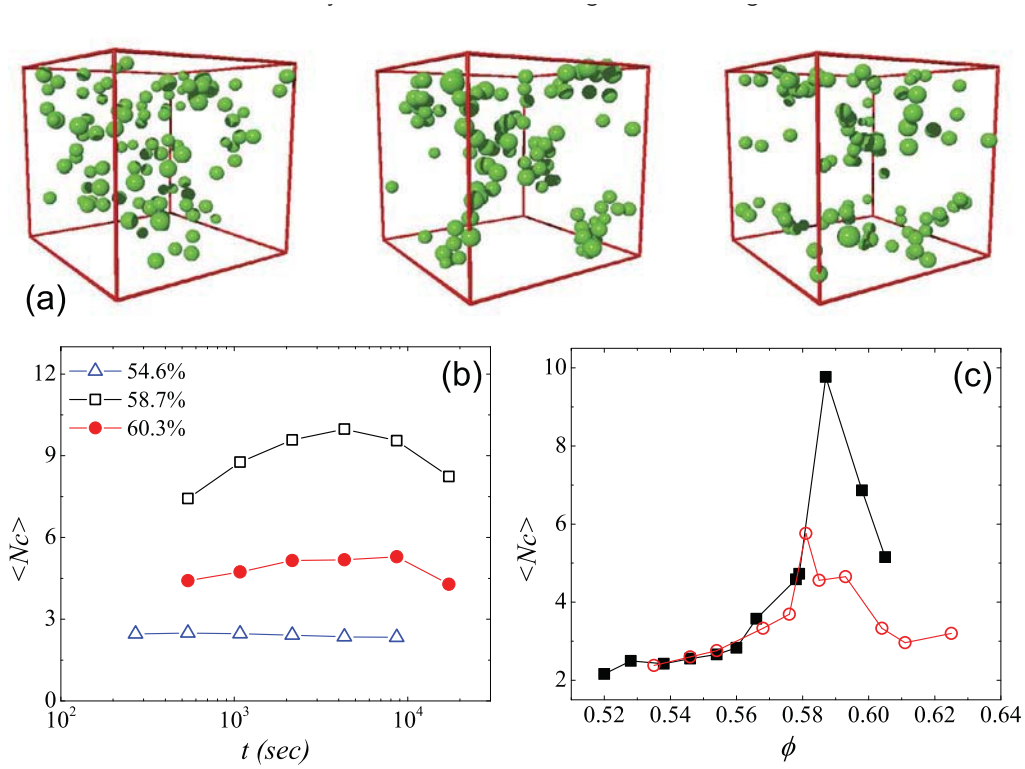

Figure 4. (a) Identification of fast particles in the microscopy experiments at different volume fractions: from left to right $\phi = 54.6\%$, $\phi = 58.7\%$ and $\phi = 60.4\%$ respectively for $t = 270\,\mathrm{s}$, $4320\,\mathrm{s}$, $8640\,\mathrm{s}$. (b) Mean cluster size from experiments as a function of time for different samples with volume fraction of 54.6%, 58.7% and 60.4%. Lines are guides to the eye. (c) Mean cluster size of fast particles as a function of the volume fraction ϕ. Closed squares: experiments; open circles: simulations.

and simulations. The agreement is striking in the whole investigated range of packing fractions. We thus analyze the concentration dependence of the minima and maxima of the $g(r)$ across the glass transition. The results are shown in figure 5(b) for experiments and simulations. For the latter, the structural properties above ϕ_g have been obtained both by averaging over a single run (as for the experimental data) and by averaging over 100 independent runs at a fixed waiting time $t_w = 2500$, to eliminate the effects of aging in the sample. The two sets of data are displayed with different colours in figure 5(b), showing that the results are similar. The main interesting feature that we find is the non-monotonic behaviour of the peaks of the $g(r)$. While the first peak seems to be barely influenced by the presence of the glass transitions, the second and the third peak together with the first three dips of the $g(r)$ display a clear change at ϕ_g. In fact we find that their amplitudes increase (peaks) or decrease (dips) on approaching the glass transition, saturating above ϕ_g meaning that the long-range structure remains unchanged by further compressing the emulsion. Differently, the behaviour of the first peak shows some changes within the first shell even beyond ϕ_g and seems to saturate only close to the jamming volume fraction [44]. This is consistent with the behaviour found in other soft particles

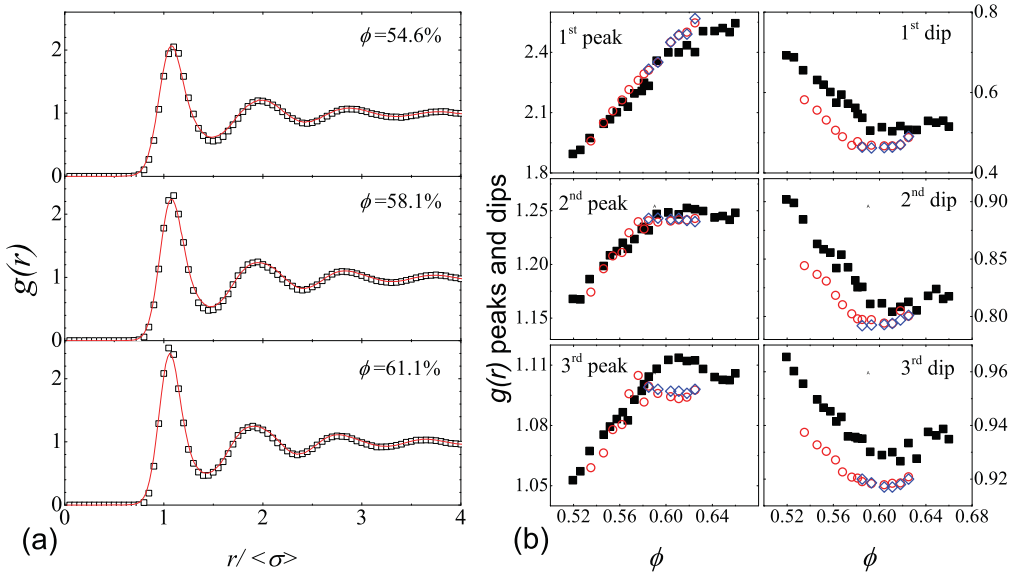

Figure 5. (a) Radial distribution function $g(r)$ of soft spheres for three volume fractions ϕ. Symbols denote experimental data for emulsions from confocal microscopy measurements, lines denote results from Brownian dynamics simulations. (b) Peak (left panel) and dip (right panel) amplitudes of $g(r)$ versus the volume fraction. Experiments: full squares. Simulations: open symbols. Circles show results obtained by averaging over a single run; diamonds show results obtained by averaging over 100 independent runs at time $t_w = 2500$.

[62, 63] such as PNIPAM particles [64] and granular materials [65] close to jamming. In those cases a maximum in the first peak of the $g(r)$ has been predicted and experimentally observed as a structural signature of the jamming transition [64, 66, 67]. Our data is consistent with these previous studies. However, due to the onset of coalescence under significant droplet compression we cannot access deeply jammed samples ($\phi > 66\%$). The limited stability under compression is a trade-off when optimizing the emulsion systems for buoancy and index matching conditions. At and below ϕ_J ($\sim$64.2%) we do not observe coalescence after more than one year.

The increase of the peaks and the decrease of all the dips of the $g(r)$ is related to the fact that, on increasing the volume fraction, particles tends to organize in better defined shells displaying a kind of 'amorphous order' [24] that needs to be quantified. This picture can be captured by looking at those parameters that probe the local structure of the system. One parameter is the average number of neighbors.

There are different ways to determine the number of nearest neighbours. One possibility is to define a cut-off distance, such as the first minimum of the $g(r)$, $r_{\min}$, and count all the neighbours within that distance from a specific particle $N_{\text{coord}} = 4\pi\rho \int_0^{r_{\min}} r^2 g(r)$. In that case the number of neighbours N_{coord} is called coordination number. However, such a definition depends on the value of the cut-off that changes in dependence of the volume fraction. Here we implement a different approach. We consider two particles as neighbours if they share a wall of a Voronoi cell. This way, the result is unique and parameter free since it is based only on geometrical considerations. The Voronoi tessellation allows not only to count the number of neighbours but also to determine

geometric properties of the cells as we will show later. The trends found in simulations and experiment are exactly the same and, except for a small shift, the data sets for N follow the same trend as shown in figure 6(a).

The concentration dependence of the average number of neighbours N shown in figure 6(a), reveals a clear change around ϕ_g. When approaching ϕ_g the number of neighbours decreases. Above ϕ_g the average number of neighbours saturates close to the value predicted for random close packing $N = 14.3$ [44]. These observations can be rationalized by considering the evolution of the dips and peaks in the radial distribution function. Below ϕ_g the boundary between the first and the second neighbouring shell is shallow and the average number of neighbours found is thus larger. As the volume fraction increases, the two shells become well separated (the first dip of the $g(r)$ decreases) and, as a consequence, the average number of neighbours decreases. For $\phi > \phi_g$ the first dip and all higher order dips and peaks saturate which is consistent with a constant number of neighbours in this regime. For comparison, the coordination number N_{coord}, extracted from the simulation data, is found to remain almost constant for $\phi < \phi_g$ and sharply decreases to a smaller value above the transition.

4.2.2. Isoperimetric quotient The isoperimetric quotient IQ [68] is an interesting measure that describes the similarity of a Voronoi cell to a sphere, and as such it is sensitive to shape changes of the cells. For an individual particle i, $IQ_i = 36\pi V_i^2/S_i^3$ where V_i and S_i are the volume and the surface area of the Voronoi cell of particle i. IQ_i is dependent on the configurations of the nearest neighbors, including the orientation and separation. With IQ we denote the average of IQ_i over all the particles. The evolution of IQ as a function of the volume fraction ϕ is shown in figure 6(b). We find that the IQ parameter increases up to ϕ_g indicating that the particles pack more homogeneously and thus tend to form more spherical Voronoi cells. Once the glass transition is approached, the packing geometry cannot be improved any further since an efficient particle rearrangement process is lacking. The saturation of N and IQ in the glass clearly shows that the geometrically configurations are frozen in and the only remaining process is the compression of the preformed cages until random close packing or jamming is reached at $\phi \to \phi_J$.

4.2.3. Orientational correlation length Previous studies have suggested that dynamical heterogeneities are related to the emergence of a medium range crystalline order [27, 29, 34] in weakly polydisperse systems highlighted by a growing bond-orientational correlation length. Although such correlation has been found to grow in a 'critical-like fashion', i.e. can be well fitted with some diverging law, the correlation lengths observed are typically limited to few particle diameters only. To investigate the presence of crystalline ordering in our moderately polydisperse emulsions, we use the bond orientational order parameters (BOO) which provide a powerful measure of the local and extended orientational symmetries in dense liquids and glasses [69]. The BOO analysis focuses on bonds joining a particle and its neighbors. Bonds are defined as the lines that link together the centers of a particle and its nearest neighbors determined by Voronoi radical tessellation. We define the BOO l-fold symmetry of a particle k as the $2l + 1$ vector:

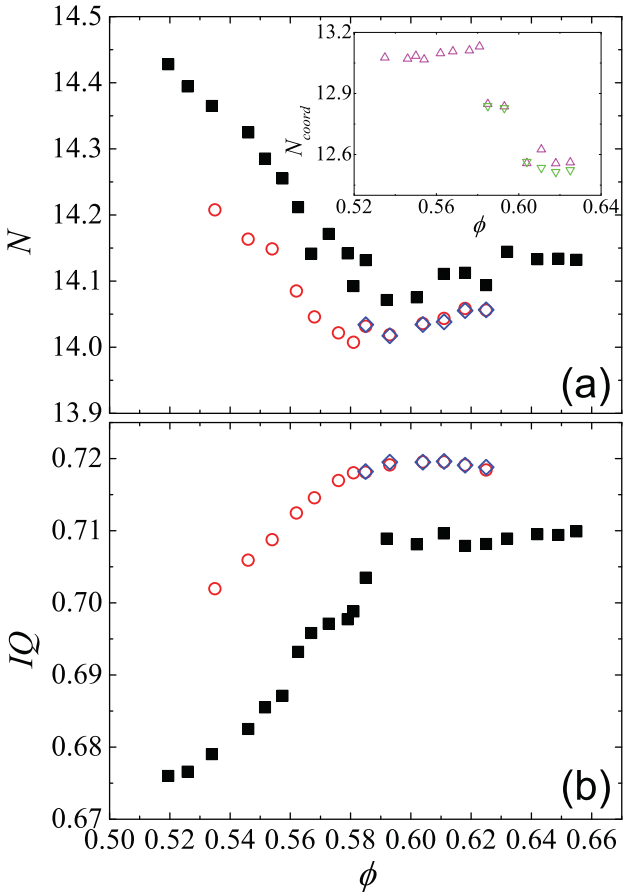

Figure 6. Analysis of the Voronoi cell and the number of neighbors: (a) average number of neighbors N and (b) isoperimetric quotient IQ as a function of the droplet volume fraction ϕ. Experiments: full squares. Simulations: open symbols. Circles are the result of a single run while diamonds are obtained by averaging over 100 independent runs at $t_{\rm w} = 2500$. Inset in (a): coordination number $N_{\rm coord}$ from simulation data. Up triangles are the result of a single run while down triangles are obtained by averaging over 100 independent runs at $t_{\rm w} = 2500$.

$$q_{lm}^{k} = \frac{1}{N^{k}} \sum_{j=1}^{N^{k}} Y_{lm}(\Theta(\vec{r}_{kj}), \Phi(\vec{r}_{kj})) \tag{4}$$

where N^k is the number of bonds of particle k, $Y_{lm}(\Theta(\vec{r}_{kj}), \Phi(\vec{r}_{kj}))$ is the spherical harmonics of degree l and order m associated to each bond and $\Theta(\vec{r}_{kj})$ and $\Phi(\vec{r}_{kj})$ are polar angles of the corresponding bond measured with respect to some reference direction. Following the work of Lechner and Dellago [70] we employ the BOO coarse-grained over the neighbours, which increases the accuracy of the type of medium-range crystalline order (e.g. FCC, HCP or BCC type):

$$Q_{l}^{k} = \sqrt{\frac{4\pi}{2l+1} \sum_{m=-l}^{l} |\, Q_{lm}^{k}|^{2}} \tag{5}$$

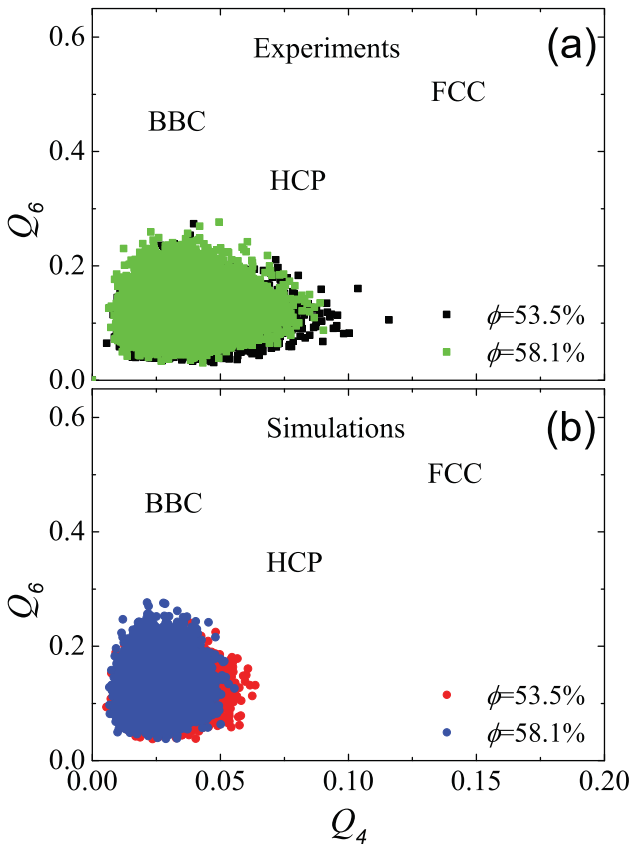

Figure 7. Correlation map of bond orientational order (BOO) parameters Q_4^k and Q_6^k at two volume fractions. The figure highlights the regions in which the order is related to three types of crystals commonly seen in colloidal system: FCC, BCC and HCP. (a) Experimental values for $\phi = 53.5\%$ and $\phi = 58.1\%$. (b) Simulations for $\phi = 53.5\%$ and $\phi = 58.1\%$ (obtained analysing 100 independent configurations at $t_w = 2500$).

with

$$Q_{lm}^k = \frac{1}{N_0^k} \sum_{j=1}^{N_0^k} q_{lm}^k(\vec{r}_{kj}) \tag{6}$$

and where N_0^k is the number of nearest neighbors of particle k including particle k itself. We first evaluate the behaviour of Q_6^k and Q_4^k which allow us to distinguish between cubic and hexagonal medium-range crystalline order. The results are shown for experiments and simulations respectively in figures 7(a) and (b). The correlation map of Q_4^k and Q_6^k reveals that, over the whole investigated range, only liquid-like structures are detected. This is due to polydispersity of our sample, which largely exceeds the known terminal polydispersity for single-phase crystallization in hard spheres [42, 43, 71]. So far, only experimental results for weakly polydisperse hard spheres (with polydispersity around 6%) have been reported, in which a medium-range crystalline order of FCC type was observed. However in our system, the reference crystal phase is not a simple

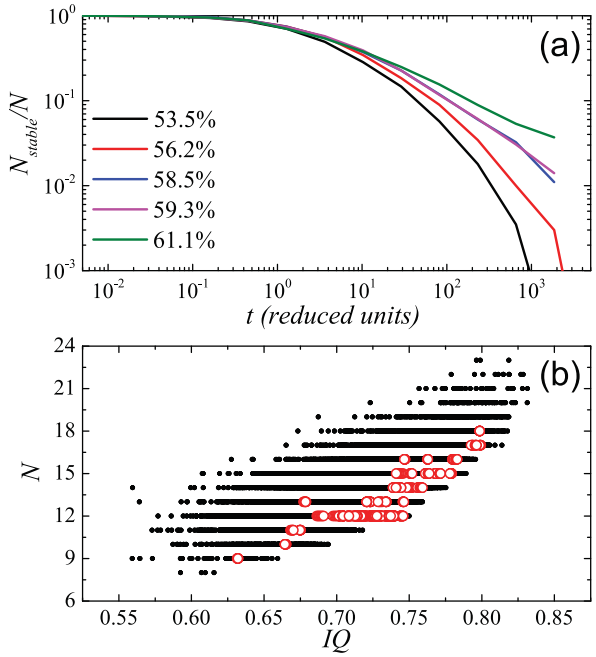

Figure 8. Decay of stable particle configurations for $\Delta t = 2500$ in reduced units. (a) Simulation data showing the fraction of stable particles as a function of time for several volume fractions. (b) Map extracted from simulations for the number of neighbors N versus the isoperimetric quotient IQ for all particles (black dots) and for stable particles (open circles).

lattice since particles should fractionate into different solids [42]. As a consequence also the BOO parameter does not reveal a clear tendency to organise in a specific crystal structure. Hence polydispersity in our case completely suppresses the formation of any crystal-like order even at the local scale.

4.3. Locally favoured structures

Locally favoured structures (LFS) are energetically favoured and as a consequence they should be long-lived in the system. LFS thus can be identified in the system by looking at the lifetime of the neighbours around a given particle. To this end we define a stable particle (i.e. by this, here, we mean droplet) i as the one that within a certain time interval Δt maintains the same neighbours n^{ij}. The latter are defined as before via the Voronoi radical tessellation. In figure 8(a) we plot for different volume fractions the typical stable particle survival rate as a function of time defined as $N_{\mathrm{stable}}/N = \langle \sum_{i<j} n^{ij}(t) n^{ij}(t+\Delta t)\rangle / N(t)$, where N is the total number of neighbours [72, 73]. We expect that, for a fixed Δt, on increasing ϕ the number of stable particles will increase since cage rearrangements become more difficult. For our analysis we fix $\Delta t = 2500$ in reduced units.

We first notice by looking at figure 8(b) that the number of neighbours of stable particles is strongly correlated with a high values of the isoperimetric quotient: this suggests that stable particles belong to a peculiar structure with a given symmetry.

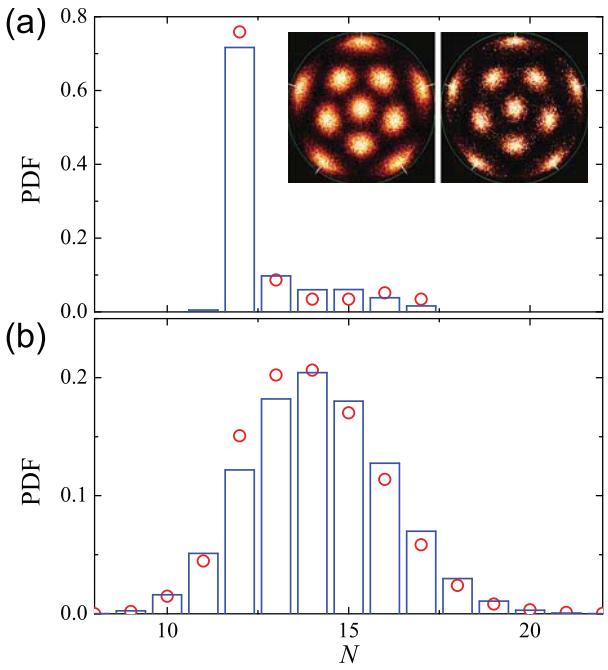

Figure 9. Distribution of the number of neighbors for $\Delta t = 2500$ in reduced units. (a) Stable particles, data averaged over $54.6\% < \phi < 60.4\%$. Experiments: bars; simulations: circles. (b) All particles at $\phi = 58.1\%$. Experiments: blue bars; simulations: red circles. Inset: bond-order diagram of $N = 12$ particle clusters identified, as described in the text and figure 9. Left: experiments. Right: simulations.

This is confirmed in figures 9 where the distribution of the number of neighbours is shown both for stable particles and for all particles. The comparison between the two distributions shows that most stable particles have exactly 12 neighbours both in simulations and in experiments, which is consistent with the idea that stable particles may form icosahedral structures. To verify this hypothesis we select stable particles with 12 neighbours and we perform a topological cluster classification (TCC) [28, 74] that allows to identify clusters that are topologically equivalent to certain reference clusters. The inset in figure 9(a) shows the bond-order diagrams of the $N = 12$ particle clusters both for experiments and simulations. The 'heat style' patterns stands for the probabilities of finding a neighbor in that direction. We start by considering that we are looking from the top of a icosahedral-structure with the central particle in the center of the figure. The central spot shows the probability of finding the top neighbor. The first five-folded spots show the probability of finding the upper layer of five neighbors. The second five-folded spots shows the lower layer. The bottom neighbor is not shown. Typical spatial icosahedral configurations of $N = 12$ clusters for different volume fractions are shown in figure 10(a).

The population of such structures is increasing when approaching some critical volume fraction around $\phi \sim 60\%$ as shown in figure 10(b). Here we plot the fraction of the population of icosahedral centers as the volume fraction crosses ϕ_g. In parallel

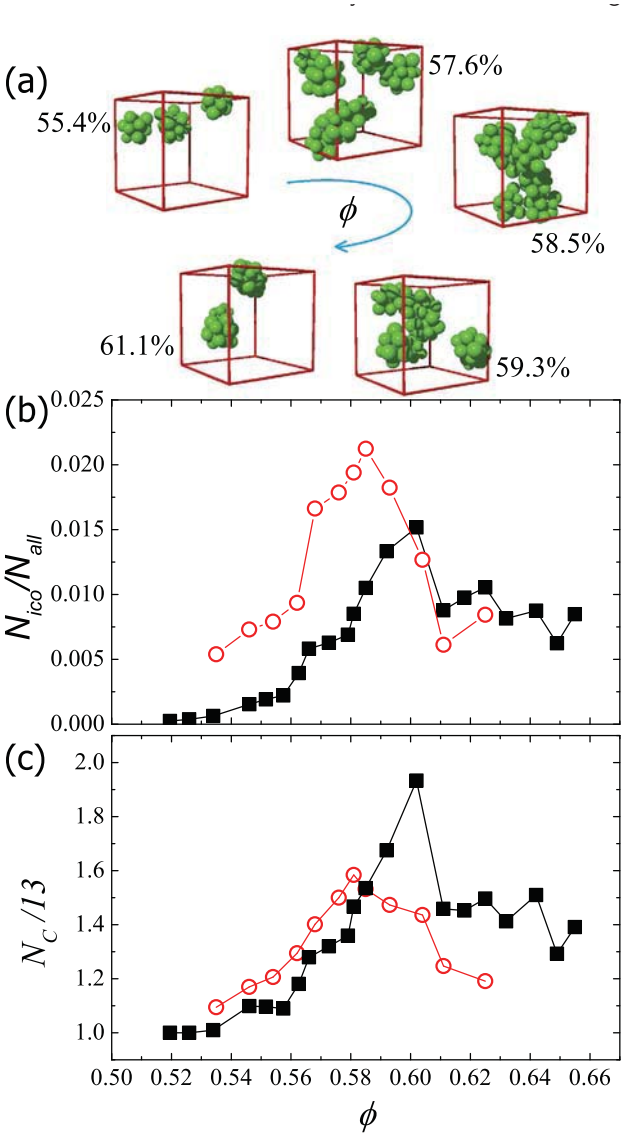

Figure 10. (a) Visualization of typical LFS for different volume fractions (simulations). (b) Number of icosahedral centers over the total number of particles. (c) Mean cluster size of icosahedral structures. Experiments: closed squares; simulations: open circles. Solid lines are guides to the eye.

the average size of connected clusters formed by icosahedral structures accordingly increases as shown in figure 10(c). Here the cluster size N_c is defined by considering all particles which are part of icosahedral structures (both centers and neighbors) and thus for an unconnected, isolated cluster $N_c/13 = 1$. Therefore $Nc/13$ shown in figure 10(c) describes the cluster size normalized by a single icosahedral structure. Above the glass transition, both the overall number and the size of icosahedral domains decreases again.

Finally in figure 11 we consider correlations between the BOO parameter Q6 and another order parameter called w_6, which is defined as

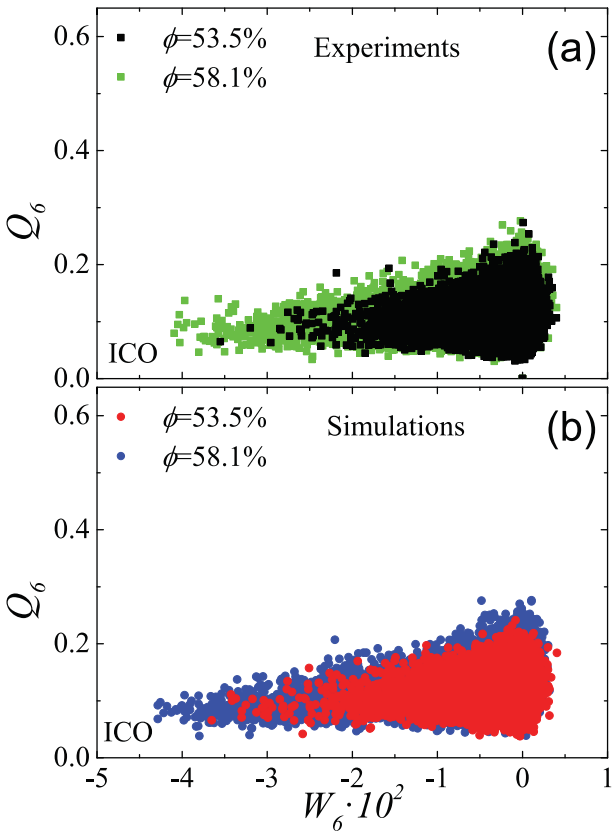

Figure 11. Correlation map of bond orientational order parameters w_6 and Q_6^k at two volume fractions. The figure highlights the regions in which the order is related to icosahedral structures. (a) Experimental values for $\phi = 53.5\%$ and $\phi = 58.1\%$. (b) Simulations for $\phi = 53.5\%$ and $\phi = 58.1\%$ (obtained analysing 100 independent configurations at $t_w = 2500$).

$$w_6(i) = \frac{\sum_{m_1+m_2+m_3} \begin{bmatrix} 6 & 6 & 6 \\ m_1 & m_2 & m_3 \end{bmatrix} q_{6m_1}(i) q_{6m_2}(i) q_{6m_3}(i)}{(\sum_{m=-6}^{6} |q_{6m}(i)|^2)^{3/2}}. \tag{7}$$

An increase of w_6 has been observed in polydisperse HS particles [34] together with the increase of crystalline order identified by a growth of the parameter Q_6. In our case, we do not observe an increase of Q_6, due to the higher polydispersity. Hence, contrary to what found in previous works on hard-spheres [34], we observe that crystalline order remains modest while icosahedral order grows when approaching the glass transition. We now need to understand if such growth is somehow related to the dynamic slowing down of the system close to ϕ_g

4.4. Link between structure and dynamics

In the previous sections, we presented evidence of both dynamical and structural signatures of the glass transition. In order to establish a link between dynamics and structure, it is worth analysing the evolution of some structural features as a function

of time. For instance we can characterize the structural and dynamical heterogeneities discussed above by some corresponding correlation lengths and search for a connection between them. To this end we estimate the correlation length associated to clusters of fast particles and to the icosahedral structures, respectively using the following relations: $\xi_{\mathrm{fast}} \propto \langle N_c^{1/3} \rangle$ and $\xi_{\mathrm{ico}} \propto \langle N_{\mathrm{ico}}^{1/3} \rangle$. In addition we evaluate the spatial correlation length ξ_6 with fold-symmetry $l = 6$ of the BOO, which can be extracted from the spatial correlation function

$$g_6(r) = \frac{4\pi}{13} \left\langle \sum_{m=-6}^{6} Q_{6m}(0) Q_{6m}(r)^* \right\rangle / \rho(r), \tag{8}$$

via the Ornstein–Zernike expression $g_6 \propto \frac{1}{r} \exp(-\frac{r}{\xi_6})$. In equation (8), $\rho(r)$ is the radial density function. The growing orientational correlation length can be characterized by a power-law function that diverges at the ideal glass transition ϕ_0 [75]

$$\xi_6 = \xi_0 [(\phi_0 - \phi)/\phi]^{-2/3}. \tag{9}$$

As suggested previously by Tanaka and coworkers [29] we can express the relaxation time τ_{D} in terms of the empirical Vogel–Fulcher–Tammann (VFT) expression, equation (2) and ξ_6 can be fitted with equation (9). Combining both, an analytic relation between τ_{D} and ξ_6 can be derived:

$$\log(\tau_{\mathrm{D}}) \propto \xi_6^{3/2}. \tag{10}$$

It is a reasonable assumption that also the other two structural correlation lengths can be described by a critical divergence analogue to equation (9) and hence we expect them to have a similar dependence on τ_{D}. In figures 12(a)–(c) we verify the suggested scaling between τ_{D} and the three structural correlations both for experiments and simulations. For $\xi_{\mathrm{ico}}^{3/2}$ and $\xi_{\mathrm{fast}}^{3/2}$ a linear relationship with $\log(\tau_{\mathrm{D}})$ is clearly confirmed. This shows that indeed the dynamics is strongly correlated with the appearance of icosahedral structures and clusters of fast particles. However, for ξ_6 such a connection is less evident. This in turn confirms that the crystalline bond orientational ordering does not play an important role in the dynamic slowing down of the system on approaching the glass transition.

In our investigation, the growth of the correlation lengths is found to be much smaller than the increase of the relaxation time. A recent work on mixtures of hard-spheres has pointed out that the dynamic correlation length extracted from the overlap function is always decoupled from the point-to-set correlation length, which represents an upper bound for the structural correlation lengths considered here [76]. Such results question the existence of a one-to-one causality relation between the growth of specific structures and the dynamical slowing down of the system close to the transition. Such correspondence has been also investigated with different tools coming from information theory [77] that confirm a connection between LFS and mobility, although such correlation turned out to be weak. Hence, although our results suggest a link between dynamical slowing down and local structural correlations even in the absence of any crystal-like ordering, the exact mechanisms connecting the growing static correlation lengths to the dynamic slowing down still remain challenging questions.

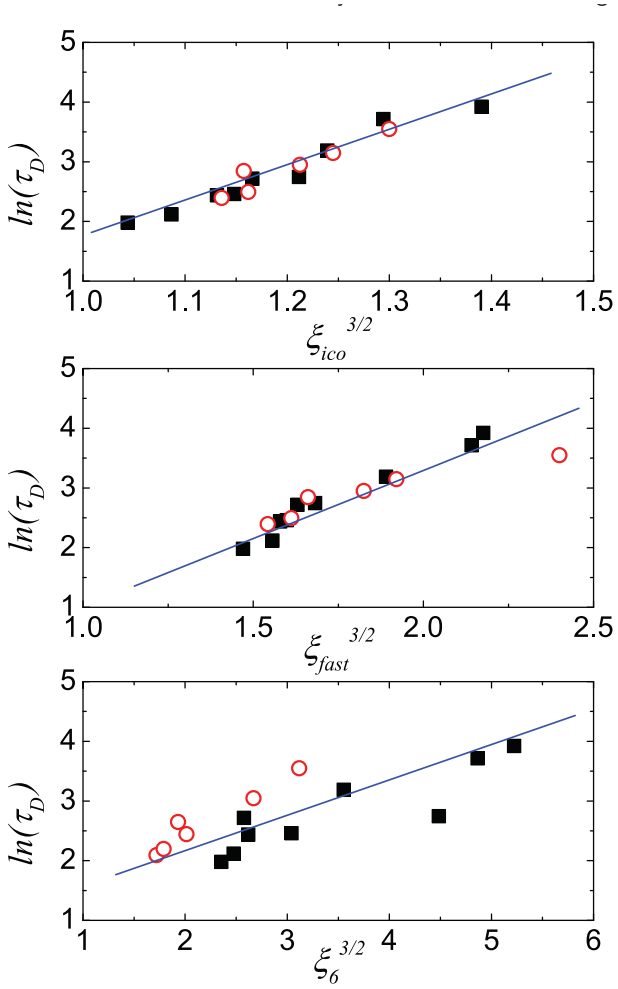

Figure 12. Natural logarithm of the α-relaxation time τ_{D} plotted versus three different spatial correlation lengths. Experiments: closed squares; simulations: open circles. (a) $\xi_{\mathrm{ico}}^{3/2}$—average size of icosahedral clusters N_{ico}; (b) $\xi_{\mathrm{fast}}^{3/2}$—average size of the fast particle clusters N_c and (c) $\xi_6^{3/2}$ correlation length derived the bond orientational order parameter Q6. Lines are guides to the eye.

5. Summary and conclusions

In summary, we have presented a comprehensive study of the glass transition in emulsions that have moderate polydispersity. We have performed 3D confocal microscopy measurements over a range of volume fractions in order to sample the system below and well above ϕ_g up to jamming. The experimental study of a system in such an extended ϕ region, crossing the glass transition and even reaching marginal jamming conditions has been previously attempted quite rarely. To obtain more detailed insights and to verify and benchmark our observations, we have compared our experimental results with a comprehensive set of Brownian dynamics simulations, finding remarkable agreement in all studied structural and dynamical properties. From this, we have demonstrated that uniform emulsions are excellent model systems for the study of the glass transition in soft colloidal systems.

In good agreement with previous work on hard spheres, we have observed that the dynamical slowing down on approaching ϕ_g is characterized by an increase of the relaxation time and the appearance of spatial and dynamical heterogeneities. The latter have been identified by the presence of fast and stable droplets that are spatially correlated. Fast droplets tend to form clusters whose size depend, not only on the distance from ϕ_g, but also on time scale considered. A close link between the maximum cluster size and the relaxation time τ_{D} was observed. This suggests that fast droplets play an important role in the structural relaxation of the system. Analogously, mechanically stable droplets arrange in long-living clusters that have peculiar geometries. By performing topological cluster classification analysis we have shown that most of these clusters are icosahedra. Moreover, their population also increases on approaching the glass transition volume fraction, approximately saturating in the glassy region. The thorough investigation of these local and average properties at volume fractions below and above ϕ_g allowed us to follow the behaviour of structural and dynamical properties over a wide range, in- and out-of-equilibrium, finding that their all relevant parameters show a peak/dip or saturate at a maximum/minimum at ϕ_g. We have also investigated whether the presence of a crystalline order exists and can be linked to the other structural signatures. Contrary to previous investigations on weakly polydisperse hard spheres, in our emulsion, which has a moderate polydispersity of about 12%, the BOO parameters Q_6 and Q_4 do not increase either on approaching the transition or even above ϕ_g; so, we do not observe signatures for the onset of crystallization or of locally ordered crystal-like regions. Thus, we have been able to establish a clear link between growing structural correlation lengths and relaxation times, thereby confirming the existence of simultaneous structural and dynamical signatures of the glass transition even in the absence of the tendency to crystallize. Our results thus generalize the picture of heterogeneities occurring at the glass transition to the experimentally relevant case of polydisperse colloids and provide evidence that emulsions are a particularly advantageous model system for testing numerical and theoretical predictions.

Acknowledgments

This research was supported by the Swiss National Science Foundation through project number 149867 and through the National Center of Competence in Research (NCCR) 'Bio-Inspired Materials' (CZ, FS), by the European Research Council through project MIMIC, ERC Consolidator Grant number 681597 (NG, EZ), and by MIUR through Futuro in Ricerca project ANISOFT number RBFR125H0M (NG, EZ). TGM acknowledges support from UCLA.

Appendix

The expression for the mean square displacement can be obtained assuming that the movement of particles in one direction is composed of two types of motions: rattling within the cage, and an inter-cage motion, such as hopping between different cages. Thus, the total displacement can be considered as the sum of the inside cage term c and an escape term related to the cage rearrangement h: $\delta x = c + h$. We assume here

that the two events are uncorrelated, therefore the 1D mean square displacement is $\langle \delta x^2 \rangle = \langle c^2 \rangle + \langle h^2 \rangle$. It is reasonable to assume that the probability of finding a particle having distance c from the center of the cage follows a Gaussian distribution $P(c) = N(0, \epsilon^2)$ with variance equal to the square of the cage size, from which follows that $\langle c^2 \rangle = \epsilon^2$. Analogously, the escape distance follows a Gaussian distribution $P(h) = N(0, \zeta^2)$ where ζ is the characteristic cage-cage hopping size. Assuming that cage rearrangement is an independent event then the distribution of the number of cage rearrangement events k follows the Poisson distribution: $P(k) = \lambda^k e^{-\lambda}/k!$ where $\lambda = t/\tau$ and τ is the lifetime of the cage. It follows that $\langle h^2 \rangle = \sum_{k=1}^{\infty} \lambda^k e^{-\lambda}/k!\ h_k^2$, where h_k is the expected displacement after k cage rearrangements and, again, it follows a Gaussian distribution with zero mean and variance $k\zeta^2$. Then $\langle h_k^2 \rangle = k\zeta^2$, and $\langle h^2 \rangle = \lambda\zeta^2$. Following the previous considerations, we can write the 3D mean square displacement as $\langle \delta r^2 \rangle = 3\langle \delta x^2 \rangle = 3[1 + (\eta/\tau)t]\epsilon^2 = 3(1 + t/\tau_{\mathrm{D}})\epsilon^2$ with $\eta = \zeta^2/\epsilon^2$. Note that we have defined the relaxation time of the system as $\tau_{\mathrm{D}} = (\tau/\eta)$ and $3\epsilon^2/\tau_{\mathrm{D}}$ is by definition six times the diffusion coefficient of the system. By interpolating the mean square displacements with the expression derived above, we are able to extract D and τ_{D} at several packing fractions ϕ.

References

[1] Petsev D N 2004 *Emulsions: Structure, Stability and Interactions: Structure, Stability and Interactions* vol 4 (London: Academic)

[2] Vlassopoulos D and Cloitre M 2014 Tunable rheology of dense soft deformable colloids *Curr. Opin. Colloid Interface Sci.* **19** 561–74

[3] Goyon J, Colin A, Ovarlez G, Ajdari A and Bocquet L 2008 Spatial cooperativity in soft glassy flows *Nature* **454** 84–7

[4] Jorjadze I, Pontani L-L and Brujic J 2013 Microscopic approach to the nonlinear elasticity of compressed emulsions *Phys. Rev. Lett.* **110** 048302

[5] Scheffold F, Wilking J N, Haberko J, Cardinaux F and Mason T G 2014 The jamming elasticity of emulsions stabilized by ionic surfactants *Soft Matter* **10** 5040–4

[6] Torquato S, Truskett T M and Debenedetti P G 2000 Is random close packing of spheres well defined? *Phys. Rev. Lett.* **84** 2064

[7] Liu A J and Nagel S R 2010 The jamming transition and the marginally jammed solid *Annu. Rev. Condens. Matter Phys.* **1** 347–69

[8] Mizuno H, Silbert L E and Sperl M 2016 Spatial distributions of local elastic moduli near the jamming transition *Phys. Rev. Lett.* **116** 068302

[9] Mewis J and Wagner N J 2012 *Colloidal Suspension Rheology* (Cambridge: Cambridge University Press)

[10] Mason T G, Bibette J and Weitz D A 1995 Elasticity of compressed emulsions *Phys. Rev. Lett.* **75** 2051

[11] Mason T G, Lacasse M-D, Grest G S, Levine D, Bibette J and Weitz D A 1997 Osmotic pressure and viscoelastic shear moduli of concentrated emulsions *Phys. Rev.* E **56** 3150

[12] Jop P, Mansard V, Chaudhuri P, Bocquet L and Colin A 2012 Microscale rheology of a soft glassy material close to yielding *Phys. Rev. Lett.* **108** 148301

[13] Paredes J, Michels M A J and Bonn D 2013 Rheology across the zero-temperature jamming transition *Phys. Rev. Lett.* **111** 015701

[14] Scheffold F, Cardinaux F and Mason T G 2013 Linear and nonlinear rheology of dense emulsions across the glass and the jamming regimes *J. Phys.: Condens. Matter* **25** 502101

[15] Crassous J J, Siebenbürger M, Ballauff M, Drechsler M, Henrich O and Fuchs M 2006 Thermosensitive core-shell particles as model systems for studying the flow behavior of concentrated colloidal dispersions *J. Chem. Phys.* **125** 204906

[16] Mason T G, Gang H and Weitz D A 1997 Diffusing wave spectroscopy measurements of viscoelasticity of complex fluids *J. Opt. Soc. Am.* A **14** 139–49

[17] Gang H, Krall A H, Cummins H Z and Weitz D A 1999 Emulsion glasses: a dynamic light-scattering study *Phys. Rev.* E **59** 715–21
[18] Mason T G and Scheffold F 2014 Crossover between entropic and interfacial elasticity and osmotic pressure in uniform disordered emulsions *Soft Matter* **10** 7109–16
[19] Golde S, Palberg T and Schöpe H J 2016 Correlation between dynamical and structural heterogeneities in colloidal hard-sphere suspensions *Nat. Phys.* **12** 712
[20] Weeks E R, Crocker J C, Levitt A C, Schofield A and Weitz D A 2000 Three-dimensional direct imaging of structural relaxation near the colloidal glass transition *Science* **287** 627–31
[21] Berthier L, Biroli G, Bouchaud J P, Cipelletti L and van Saarloos W 2011 *Dynamical Heterogeneities in Glasses, Colloids, and Granular Media* (Oxford: Oxford University Press)
[22] Zhao K and Mason T G 2015 Shape-designed frustration by local polymorphism in a near-equilibrium colloidal glass *Proc. Natl Acad. Sci.* **112** 12063–8
[23] Kirkpatrick T R, Thirumalai D and Wolynes P G 1989 Scaling concepts for the dynamics of viscous liquids near an ideal glassy state *Phys. Rev.* A **40** 1045
[24] Biroli G, Bouchaud J-P, Cavagna A, Grigera T S and Verrocchio P 2008 Thermodynamic signature of growing amorphous order in glass-forming liquids *Nat. Phys.* **4** 771–5
[25] Toninelli C, Wyart M, Berthier L, Biroli G and Bouchaud J P 2005 Dynamical susceptibility of glass formers: Contrasting the predictions of theoretical scenarios *Phys. Rev.* E **71** 041505
[26] Hedges L O, Jack R L, Garrahan J P and Chandler D 2009 Dynamic order-disorder in atomistic models of structural glass formers *Science* **323** 1309–13
[27] Kawasaki T, Araki T and Tanaka H 2007 Correlation between dynamic heterogeneity and medium-range order in two-dimensional glass-forming liquids *Phys. Rev. Lett.* **99** 215701
[28] Watanabe K and Tanaka H 2008 Direct observation of medium-range crystalline order in granular liquids near the glass transition *Phys. Rev. Lett.* **100** 158002
[29] Tanaka H, Kawasaki T, Shintani H and Watanabe K 2010 Critical-like behaviour of glass-forming liquids *Nat. Mater.* **9** 324–31
[30] Royall C P and Williams S R 2015 The role of local structure in dynamical arrest *Phys. Rep.* **560** 1–75
[31] Frank F C 1952 Supercooling of liquids *Proc. R. Soc. London* A 43–6
[32] Tarjus G, Kivelson S A, Nussinov Z and Viot P 2005 The frustration-based approach of supercooled liquids and the glass transition: a review and critical assessment *J. Phys.: Condens. Matter* **17** R1143
[33] Leocmach M, Russo J and Tanaka H 2013 Importance of many-body correlations in glass transition: an example from polydisperse hard spheres *J. Chem. Phys.* **138** 12A536
[34] Leocmach M and Tanaka H 2012 Roles of icosahedral and crystal-like order in the hard spheres glass transition *Nat. Commun.* **3** 974
[35] Poon W C K, Weeks E R and Royall C P 2012 On measuring colloidal volume fractions *Soft Matter* **8** 21–30
[36] Pellet C and Cloitre M 2016 The glass and jamming transitions of soft polyelectrolyte microgel suspensions *Soft Matter* **12** 3710–20
[37] Mohanty P S, Paloli D, Crassous J J, Zaccarelli E and Schurtenberger P 2014 Effective interactions between soft-repulsive colloids: experiments, theory, and simulations *J. Chem. Phys.* **140** 094901
[38] Vlassopoulos D 2004 Colloidal star polymers: models for studying dynamically arrested states in soft matter *J. Polym. Sci.* B **42** 2931–41
[39] Mattsson J, Wyss H M, Fernandez-Nieves A, Miyazaki K, Hu Z, Reichman D R and Weitz D A 2009 Soft colloids make strong glasses *Nature* **462** 83–6
[40] Gasser U, Hyatt J S, Lietor-Santos J-J, Herman E S, Lyon L A and Fernandez-Nieves A 2014 Form factor of pnipam microgels in overpacked states *J. Chem. Phys.* **141** 034901
[41] Scotti A 2015 Phase behavior of binary mixtures and polydisperse suspensions of compressible spheres *PhD Thesis* ETH-Zürich
[42] Fasolo M and Sollich P 2003 Equilibrium phase behavior of polydisperse hard spheres *Phys. Rev. Lett.* **91** 068301
[43] Zaccarelli E, Valeriani C, Sanz E, Poon W C K, Cates M E and Pusey P N 2009 Crystallization of hard-sphere glasses *Phys. Rev. Lett.* **103** 135704
[44] Zhang C, O'Donovan C B, Corwin E I, Cardinaux F, Mason T G, Möbius M E and Scheffold F 2015 Structure of marginally jammed polydisperse packings of frictionless spheres *Phys. Rev.* E **91** 032302
[45] Bibette J 1991 Depletion interactions and fractionated crystallization for polydisperse emulsion purification *J. Colloid Interface Sci.* **147** 474–8
[46] Brujic J 2004 *Experimental Study of Stress Transmission Through Particulate Matter* (Cambridge: University of Cambridge)
[47] Rycroft C 2009 *Voro++: a Three-Dimensional Voronoi Cell Library in c++* (Berkeley, CA: Lawrence Berkeley National Laboratory)

[48] Desmond K W and Weeks E R 2014 Influence of particle size distribution on random close packing of spheres *Phys. Rev.* E **90** 022204
[49] Lacasse M-D, Grest G S, Levine D, Mason T G and Weitz D A 1996 Model for the elasticity of compressed emulsions *Phys. Rev. Lett.* **76** 3448
[50] Berthier L and Witten T A 2009 Compressing nearly hard sphere fluids increases glass fragility *Europhys. Lett.* **86** 10001
[51] Ikeda A, Berthier L and Sollich P 2012 Unified study of glass and jamming rheology in soft particle systems *Phys. Rev. Lett.* **109** 018301
[52] Ikeda A, Berthier L and Sollich P 2013 Disentangling glass and jamming physics in the rheology of soft materials *Soft Matter* **9** 7669–83
[53] Russo J, Tartaglia P and Sciortino F 2009 Reversible gels of patchy particles: role of the valence *J. Chem. Phys.* **131** 014504
[54] Seth J R, Cloitre M and Bonnecaze R T 2006 Elastic properties of soft particle pastes *J. Rheol.* **50** 353–76
[55] Zaccarelli E, Liddle S M and Poon W C K 2015 On polydispersity and the hard sphere glass transition *Soft Matter* **11** 324–30
[56] Doliwa B and Heuer A 1998 Cage effect, local anisotropies, and dynamic heterogeneities at the glass transition: a computer study of hard spheres *Phys. Rev. Lett.* **80** 4915
[57] Weeks E R and Weitz D A 2002 Properties of cage rearrangements observed near the colloidal glass transition *Phys. Rev. Lett.* **89** 095704
[58] Zhang C 2015 Confocal microscopy of the glass and the jamming transition in microscale emulsions *PhD Thesis* University of Fribourg, Switzerland
[59] Kob W, Donati C, Plimpton S J, Poole P H and Glotzer S C 1997 Dynamical heterogeneities in a supercooled lennard-jones liquid *Phys. Rev. Lett.* **79** 2827
[60] Donati C, Glotzer S C, Poole P H, Kob W and Plimpton S J 1999 Spatial correlations of mobility and immobility in a glass-forming lennard-jones liquid *Phys. Rev.* E **60** 3107
[61] Kegel W K and van Blaaderen A 2000 Direct observation of dynamical heterogeneities in colloidal hard-sphere suspensions *Science* **287** 290–3
[62] Silbert L E, Liu A J and Nagel S R 2006 Structural signatures of the unjamming transition at zero temperature *Phys. Rev.* E **73** 041304
[63] Jacquin H, Berthier L and Zamponi F 2011 Microscopic mean-field theory of the jamming transition *Phys. Rev. Lett.* **106** 135702
[64] Zhang Z, Xu N, Chen D T N, Yunker P, Alsayed A M, Aptowicz K B, Habdas P, Liu A J J, Nagel S R and Yodh A G 2009 Thermal vestige of the zero-temperature jamming transition *Nature* **459** 230–3
[65] Cheng X 2010 Experimental study of the jamming transition at zero temperature *Phys. Rev.* E **81** 031301
[66] Paloli D, Mohanty P S, Crassous J J, Zaccarelli E and Schurtenberger P 2013 Fluid-solid transitions in soft-repulsive colloids *Soft Matter* **9** 3000–4
[67] Liu A J, Nagel S R, Van Saarloos W and Wyart M 2010 *Dynamical Heterogeneities in Glasses, Colloids, and Granular Media* (Oxford: Oxford University Press)
[68] Damasceno P F, Engel M and Glotzer S C 2012 Predictive self-assembly of polyhedra into complex structures *Science* **337** 453–7
[69] Steinhardt P J, Nelson D R and Ronchetti M 1983 Bond-orientational order in liquids and glasses *Phys. Rev.* B **28** 784
[70] Lechner W and Dellago C 2008 Accurate determination of crystal structures based on averaged local bond order parameters *J. Chem. Phys.* **129** 114707
[71] Martinez V A, Zaccarelli E, Sanz E, Valeriani C and van Megen W 2014 Exposing a dynamical signature of the freezing transition through the sound propagation gap *Nat. Commun.* **5** 5503
[72] Puertas A M, Fuchs M and Cates M E 2003 Simulation study of nonergodicity transitions: gelation in colloidal systems with short-range attractions *Phys. Rev.* E **67** 031406
[73] Zaccarelli E and Poon W C K 2009 Colloidal glasses and gels: the interplay of bonding and caging *Proc. Natl Acad. Sci.* **106** 15203–8
[74] Malins A, Williams S R, Eggers J and Royall C P 2013 Identification of structure in condensed matter with the topological cluster classification *J. Chem. Phys.* **139** 234506
[75] Onuki A 2002 *Phase Transition Dynamics* (Cambridge: Cambridge University Press)
[76] Charbonneau P and Tarjus G 2013 Decorrelation of the static and dynamic length scales in hard-sphere glass formers *Phys. Rev.* E **87** 042305
[77] Jack R L, Dunleavy A J and Royall C P 2014 Information-theoretic measurements of coupling between structure and dynamics in glass formers *Phys. Rev. Lett.* **113** 095703